

# Effects of Gd, Y, and La Rare-Earth Elements on the Microstructural Stability and Elevated-Temperature Mechanical Properties of AZ81 Magnesium Alloy



SEYED MASOUD ASHRAFIZADEH and REZA MAHMUDI

The effects of separate additions of 1 wt pct Gd, Y, and La rare-earth (RE) elements on the microstructural stability and strength of a cast AZ81 alloy were investigated in the as-cast and annealed conditions. Scanning electron microscopy (SEM), energy-dispersive spectroscopy (EDS), differential scanning calorimetry (DSC), X-ray diffraction (XRD), and optical microscopy (OM) analyses along with shear punch testing (SPT) were employed to characterize the microstructural stability and mechanical properties of the studied alloys. The main microstructural constituent in the AZ81 base alloy,  $Mg_{17}Al_{12}$  intermetallic phase, showed a relatively low thermal stability, resulting in a significant strength decline at high temperatures. The incorporation of the RE elements into the base alloy not only refined the microstructure but also improved the thermal stability and high-temperature mechanical properties of the RE-containing alloys. The observed enhancement in both stability and shear strength was attributed to the reduction in the volume fraction of  $\beta$ - $Mg_{17}Al_{12}$  and formation of the thermally stable  $Al_2Gd$ ,  $Al_2Y$ , and  $Al_{11}La_3$  intermetallic particles, which suppress the grain growth throughout the annealing process. Among the employed RE elements, La was found to be the most effective one in the retention of the initial fine microstructure as well as ultimate shear strength after long-term annealing at 400 °C. This is believed to be caused by the higher number density and more uniform dispersion of the  $Al_{11}La_3$  particles in the Mg matrix in comparison with the  $Al_2Gd$  and  $Al_2Y$  particles, which showed a more sparse distribution of some agglomerated particles.

<https://doi.org/10.1007/s11661-019-05471-y>

© The Minerals, Metals & Materials Society and ASM International 2019

## I. INTRODUCTION

AMONG various Mg alloys, the Mg-Al-Zn series, designated as AZ alloys, exhibit appropriate mechanical properties and corrosion resistance.<sup>[1-3]</sup> These alloys possess interesting characteristics including low-specific gravity, high-specific strength and stiffness, and excellent machinability. Due to such admiring properties, these alloys have found practical uses in automotive industries. One of the most important shortcomings in the application of these alloys, however, is their pronounced softening, and thus, relatively low strength and creep resistance at high working temperatures. Therefore, designing Mg-based alloys with high-thermal stability at

elevated temperatures has attracted the attention of several researchers in this field.<sup>[4,5]</sup>

One of the feasible means of overcoming the above-mentioned deficiency is the incorporation of some alloying elements that can form thermally stable second-phase particles.<sup>[6-11]</sup> Accordingly, a notable progress has occurred by the introduction of different rare-earth (RE) elements into the Mg matrix. Gadolinium (Gd) is a RE element that has recently gained a prevalent interest as an alloying element in the Mg alloys.<sup>[12]</sup> The influence of various contents of Gd on the microstructure of cast Mg has been examined. The results have shown improvements in strength values due to the formation of MgGd and  $Mg_5Gd$  particles.<sup>[13]</sup> In a separate research, the addition of 1 to 4 wt pct of Gd to an AZ21 Mg alloy has been considered. The results revealed the formation of both  $(Mg, Al)_3Gd$  phase with branch-shaped morphology as well as  $Al_2Gd$  particles with cubic shape morphology; both of which resulted in some improvements in tensile strength and creep resistance.<sup>[14]</sup> Minor addition of Gd to AZ80 alloy has indicated that in the AZ80 + 1Gd alloy, the partially agglomerated particles were mainly

SEYED MASOUD ASHRAFIZADEH and REZA MAHMUDI are with the School of Metallurgical and Materials Engineering, College of Engineering, University of Tehran, Tehran, Iran. Contact e-mail: mahmudi@ut.ac.ir

Manuscript submitted March 10, 2019.

Article published online October 10, 2019

$\text{Al}_2\text{Gd}$ .<sup>[15]</sup> In addition to particle hardening, Gd is known to strengthen the Mg matrix *via* solid solution hardening.<sup>[16]</sup> Another aspect of Gd addition to Mg-Al alloys is its grain refinement capability.<sup>[17,18]</sup>

In several researches, the effect of Y addition on the microstructure and properties of the Mg-Al-Zn alloys has been investigated. It has been reported that through addition of Y, the morphology of  $\beta\text{-Mg}_{17}\text{Al}_{12}$  phase changes and the new reinforcing phase of  $\text{Al}_2\text{Y}$  with a face center cubic (FCC) structure and cuboid morphology is formed in the  $\alpha\text{-Mg}$  matrix. The formation of the stable  $\text{Al}_2\text{Y}$  phase, with a melting point of 1536 °C, has been introduced as the main cause of improved hardness and corrosion resistance,<sup>[19–23]</sup> tensile strength,<sup>[24]</sup> and creep resistance.<sup>[25]</sup>

The most common RE elements that are used to improve the high-temperature mechanical properties of the AZ magnesium alloys are lanthanum (La) and cerium (Ce).<sup>[26,27]</sup> Mahmudi *et al.*<sup>[28]</sup> investigated the mechanical behavior and microstructural stability of AZ91 and AZ91 + 2 wt pct La-rich RE alloys. They reported that the RE-containing material had a more refined microstructure with enhanced thermal stability and strength at elevated temperatures, as compared to the base AZ91 alloy. The improved properties were ascribed to the high-thermal stability of the  $\text{Al}_{11}\text{RE}_3$  intermetallic particles and lower volume fraction of the unstable  $\beta\text{-Mg}_{17}\text{Al}_{12}$  phase. Similarly, the addition of Ce-rich mish metal to an AZ81 Mg alloy has resulted in microstructural refinement, reduction in the content of  $\beta\text{-Mg}_{17}\text{Al}_{12}$  phase, and enhancement of tensile strength of the alloy at both ambient temperature and 150 °C.<sup>[29]</sup> In another work, tensile testing of an AZ91 alloy containing 2 wt pct of Ce-rich RE elements showed no decline in the strength of the alloy at temperatures up to 150 °C.<sup>[30]</sup> Kabirian *et al.* investigated the effect of various contents of La-rich RE elements on the creep behavior of a cast AZ91 Mg alloy and reported that the best creep resistance was observed for an alloy with 2 wt pct RE element.<sup>[31]</sup> They attributed this improvement to the formation of the well-distributed acicular branch-shaped  $\text{Al}_{11}\text{RE}_3$  particles with a high melting point of 1235 °C.

In the current study, a comparative study was made on the effect of separate addition of 1 wt pct Gd, Y, and La elements on the microstructure and shear strength of the AZ81 alloy. The characteristics of the as-cast specimens as well as those exposed to high temperatures were examined throughout this study. It was also intended to evaluate the microstructural stability of the alloys through studying the behavior of the cast alloys at high temperatures to identify the most effective RE element. The strength of the alloys was determined by the shear punch testing (SPT) method, frequently employed for various cast Mg alloys.<sup>[6,7,10]</sup>

## II. EXPERIMENTAL

### A. Materials and Procedures

The base material was AZ81 Mg alloy with an actual chemical composition of Mg-7.9 wt pct Al-1.02 wt pct Zn. High-purity Mg (99.90 wt pct), Al (99.94 wt pct), and Zn

(99.95 wt pct) were used to prepare the base AZ81 alloy. The additives were either of 0.97 wt pct Gd, 1.02 wt pct Y, or 1.08 wt pct La elements, which were provided by the master alloys of Mg containing 30 wt pct of each of those elements. An electrical furnace was employed for melting purposes, where the Foseco MAGREX 36\* covering flux

---

\*MAGREX 36 is a trademark of Foseco, Staffordshire, United Kingdom.

---

was used to prevent the molten magnesium from oxidation. The weighted charges were melted at 780 °C and maintained at the same temperature for 20 minutes. The melt was then stirred for 2 minutes using a stainless steel rod for homogeneity, before being poured into a steel mold that was preheated to 150 °C. A tilt-casting set up was used for casting to avoid the occurrence of any turbulent motion of the melt. The cast bars with dimensions of  $13 \times 30 \times 150 \text{ mm}^3$  were obtained, from which slices of  $1 \times 3 \times 30 \text{ mm}^3$  were cut by an electro-discharge wire-cut machine. The final specimens were used for shear punch testing (SPT) as well as structural characterization.

### B. Microstructural Characterization

To study the microstructural stability of the alloys, some of the cast specimens were annealed at 400 °C for 0, 4, 24 and 96 hours, and water quenched at ambient temperature. The as-cast and annealed specimens were polished using a solution of 0.3  $\mu\text{m}$  alumina suspension in distilled water. Etching of the samples was conducted through submerging the specimens into an acetic picric etchant solution (15 mL acetic acid, 10 mL  $\text{H}_2\text{O}$ , 4.5 g picric acid and 65 mL ethyl alcohol) for 10 to 30 seconds at room temperature. Optical microscopy (OM) was conducted to examine the effect of elemental additions on their microstructural and thermal stabilities. Scanning electron microscopy (SEM) was carried out on both of the as-cast and annealed samples to study their microstructures as well as the chemical composition of the newly formed phases.

X-ray diffraction (XRD) analysis was performed on the as-cast and 96-hours annealed specimens to identify the phases. XRD analysis with a wavelength of 1.54056 Å and a scanning rate of 2 deg/min was used to expose the specimens to Cu  $K\alpha$  radiation. The energy-dispersive spectroscopy (EDS) analysis was carried out on the as-cast specimens to determine the concentration of the added elements in particular areas of the microstructure. Differential scanning calorimetry (DSC) was performed in a Perkin Elmer STA6000 instrument using a scanning rate of 5 °C/min under argon atmosphere to study the thermal behavior of the specimens.

### C. Shear Strength Measurements

The effects of elemental additions as well as annealing treatment on the mechanical properties of the alloys were investigated through measurement of the shear strength of the alloys by the shear punch testing (SPT) method. 1-mm-thick slices of the alloys annealed for 0,

4, 24 and 96 hours were thinned to a nominal thickness of 0.7 mm by emery paper. A fixture with a flat cylindrical punch of 3.125 mm in diameter and a receiving-hole of 3.225 mm in diameter was used for SPT. Shear punch tests were conducted in a wide temperature range of 25 to 250 °C, using a screw-driven SANTAM material testing system with a load cell of 20 kN capacity and a crosshead speed of 0.25 mm/min. By loading the specimen, the applied pressure,  $P$ , was automatically measured as a function of punch displacement. After obtaining the required data, the shear stress of the tested materials was calculated by the following equation.<sup>[32]</sup>

$$\tau = \frac{P}{\pi dt} \quad [1]$$

where  $P$  is the applied load,  $t$  is the thickness of the specimen, and  $d$  is the mean value of the punch and die diameters. Three different measurements were made in each particular condition and the average values were reported. There were only very small scatters in the measured ultimate shear strength (USS) values.

### III. RESULTS AND DISCUSSION

#### A. Microstructure and Chemical Analysis

The SEM images of the as-cast samples are exhibited in Figure 1. As can be deduced from Figure 1(a), the base AZ81 alloy possesses a dendritic structure, where some particles of  $\beta$ -Mg<sub>17</sub>Al<sub>12</sub> are distributed as a second phase within the inter-dendritic regions. Incorporation of any RE element, *i.e.* Gd, Y, and La, into the base alloy, results in some respective changes in both morphology and volume fraction of the particles (Figures 1(b) to (d)). After the addition of these elements, the dendritic microstructures are refined and their arm spacing is reduced. As such, during the solidification process, RE atoms have been driven to the solid-liquid interface, creating concentration undercooling and caused an increase in the nucleation rate that suppressed the grain growth.<sup>[33]</sup> The electronegativity values of Mg, Al, Gd, Y, and La are presented in Table I. It is evident that there is higher tendency for RE elements to form Al-RE compounds than Mg-Al particles. Moreover, among different Al-RE particles, there is a higher probability for the formation of Al-La particles than Al-Gd and Al-Y particles.

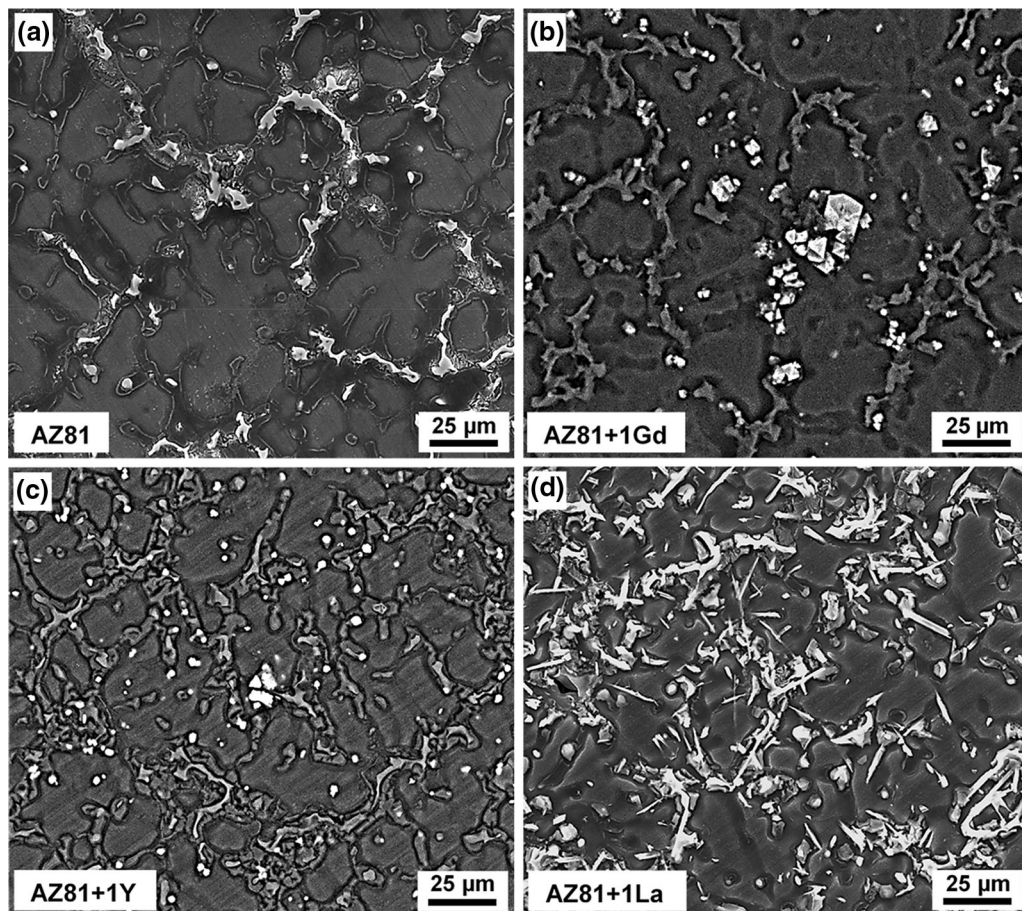


Fig. 1—SEM micrographs of the as-cast specimens (a) AZ81, (b) AZ81 + 1Gd, (c) AZ81 + 1Y, and (d) AZ81 + 1La.

**Table I. Electronegativity of Mg, Al, Gd, Y, and La Elements<sup>[34]</sup>**

Element	Electronegativity
Mg	1.31
Al	1.61
Gd	1.20
Y	1.22
La	1.10

SEM images were taken from the same alloys exhibited in Figure 1 at a higher magnification, and the EDS point analyses at a number of regions in each micrograph were conducted to identify the formed phases within the microstructure of the samples. The results of these investigations are depicted in Figure 2. Considering the EDS analysis given in the Table below each micrograph, the atomic percent of elements in different locations of the microstructure was determined

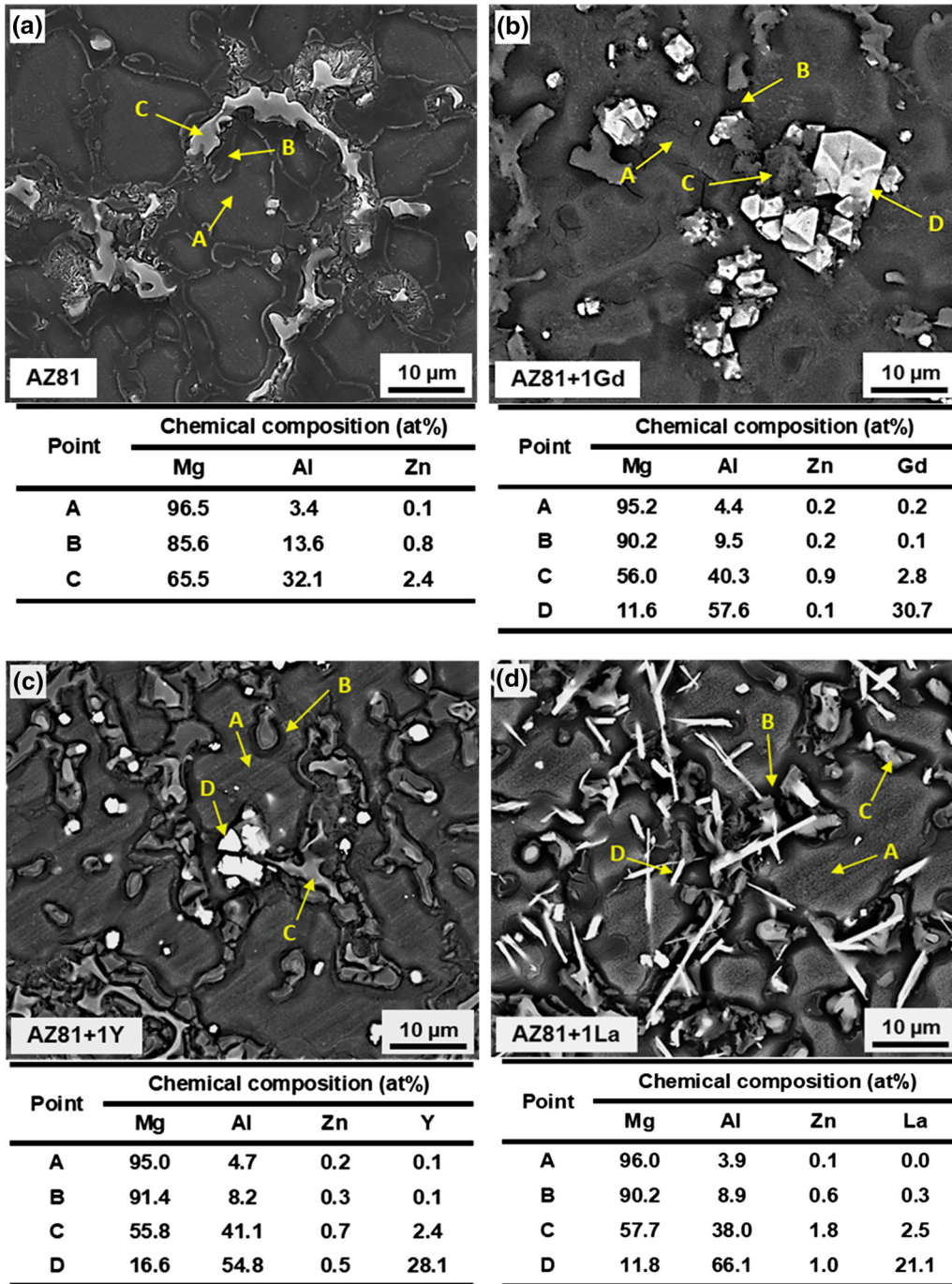


Fig. 2—SEM micrographs and EDS analysis of different points of specimens (a) AZ81, (b) AZ81 + 1Gd (c) AZ81 + 1Y, and (d) AZ81 + 1La.

and the corresponding phase was identified. Various regions of the alloys AZ81, AZ81 + 1Gd, AZ81 + 1Y, and AZ81 + 1La are shown in Figures 2(a) through (d), respectively. The lighter regions, forming the background of the images (labeled as *A*), represent  $\alpha$ -Mg dendrites, whereas the dark regions (labeled as *B*) represent the same phase supersaturated by Al, and some coarse particles (labeled as *C*) represent  $\beta$ -Mg<sub>17</sub>Al<sub>12</sub> intermetallics. The microstructure of the AZ81 + 1Gd alloy, shown in Figure 2(b), indicates that the agglomerated particles with cubic morphology (labeled as *D*) represent Al<sub>2</sub>Gd particles. In Figure 2(c), the partially agglomerated particles with a cubic morphology (labeled as *D*) represent Al<sub>2</sub>Y particles in AZ81+1Y. Finally, the microstructure of the AZ81 + 1La alloy in Figure 2(d) contains some dispersed particles with needle-shaped morphology (labeled as *D*), which are Al<sub>11</sub>La<sub>3</sub> intermetallics.

Differences in the morphology of the second-phase particles and the way they are dispersed in the alloy matrix have a significant influence on the material microstructure. This would, in turn, result in different high-temperature stabilities and mechanical properties that will be discussed in the next sections. The particles in the Gd- and Y-containing alloys with similar cuboid morphologies and melting points have resulted in almost

finer dendritic structures in comparison with the base alloy. In spite of the existing similarities between the alloys containing Y and Gd, the difference in their microstructures is due to the different levels of agglomeration of the particles; Al<sub>2</sub>Gd has a higher tendency towards agglomeration than Al<sub>2</sub>Y. This can be attributed to the heavier weight of Gd which makes the movement of these particles more difficult, and thus, a more restricted distribution is obtained.<sup>[15]</sup> In the La-containing alloy, however, due to adequate dispersion of the particles and their blade geometry, a finer dendritic structure has been formed.

### B. Microstructural Stability

Differential scanning calorimetry was conducted in the temperature range 300 °C to 500 °C to study the thermal behavior of the base and RE-containing specimens. The results of this experiment, presented as complete heating and cooling curves, are shown in Figure 3. The peaks in the heating and cooling curves correspond to the dissolution and precipitation temperatures of the  $\beta$ -Mg<sub>17</sub>Al<sub>12</sub> phase, respectively. It is evident that the dissolution temperature varies from 423.4 °C in the base alloy (Figure 3(a)) to 426.9 °C, 428.2 °C, and 434.1 °C (Figures 3(b) to (d)) for the

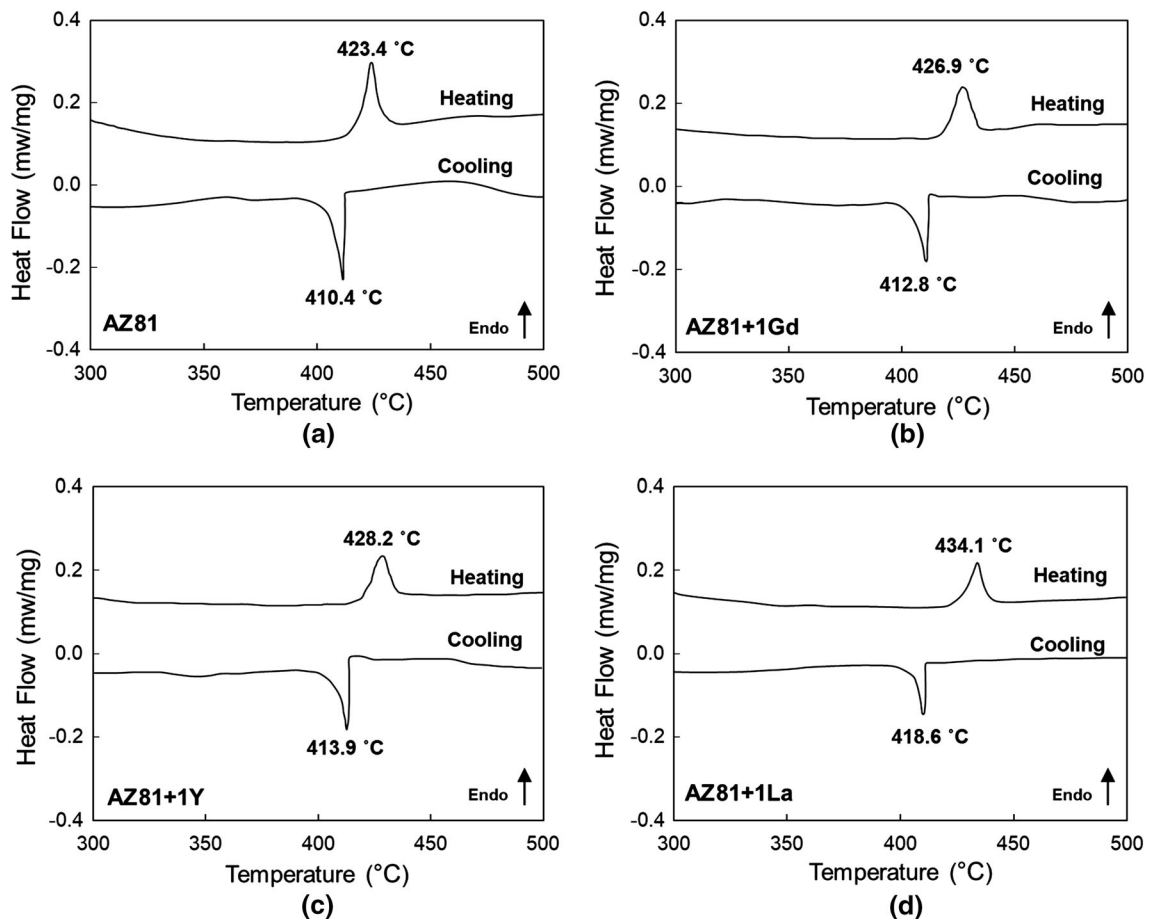


Fig. 3—DSC heating and cooling curves of (a) AZ81, (b) AZ81 + 1Gd, (c) AZ81 + Y, and (d) AZ81 + 1La alloy.

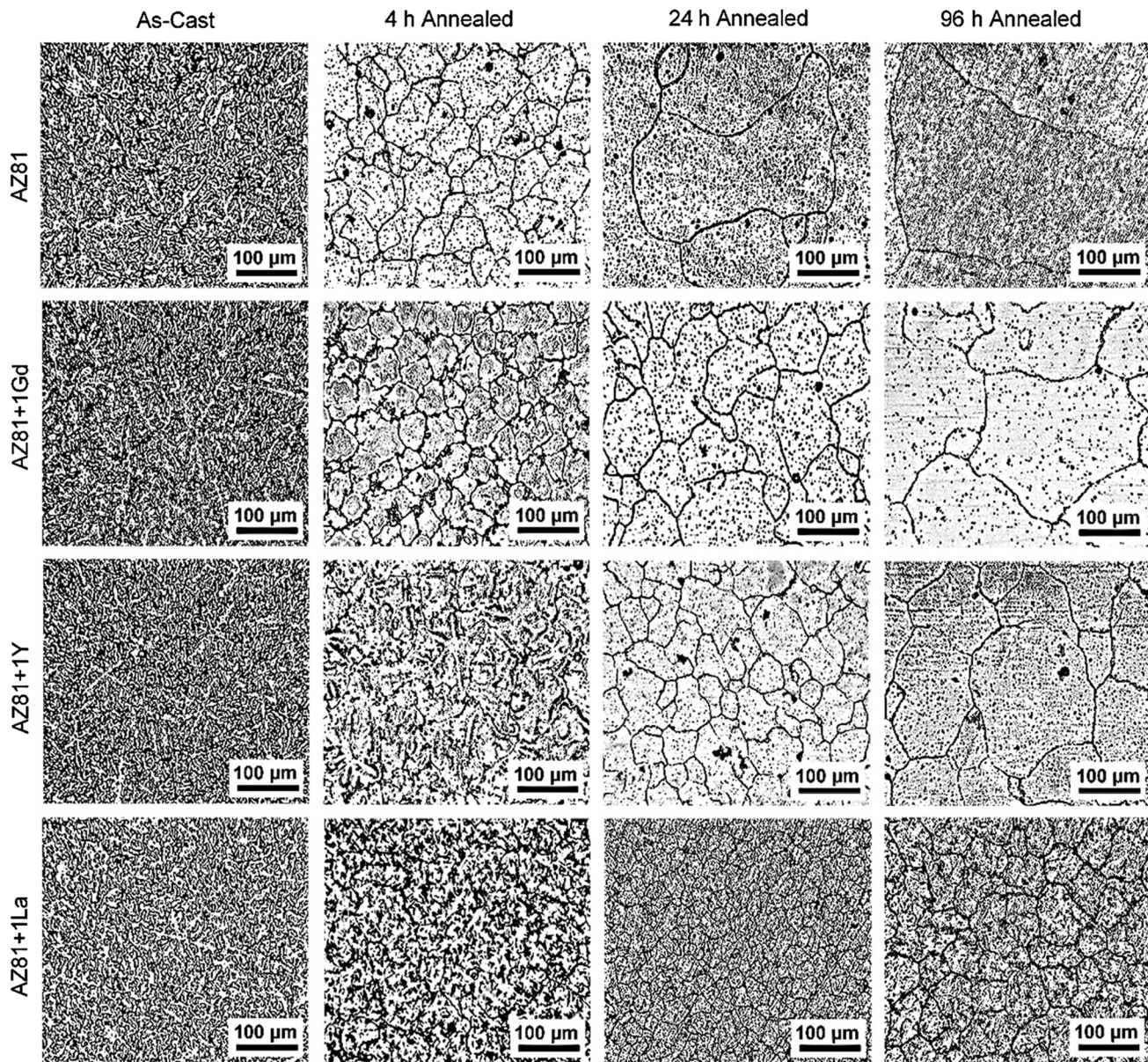


Fig. 4—Optical micrographs of the as-cast and annealed specimens of AZ81, AZ81 + 1Gd, AZ81 + 1Y, and AZ81 + 1La.

alloys containing Gd, Y, and La, respectively. The observed shift in the peak temperatures is attributed to the presence of small quantities of the RE elements within the  $\beta$ -Mg<sub>17</sub>Al<sub>12</sub> phase. The corresponding amounts of the RE elements present in the chemical compositions of the  $\beta$ -Mg<sub>17</sub>Al<sub>12</sub> phase have already been determined and demonstrated in Figures 2(b) through (d). It seems that the high melting points of the mentioned RE additives, incorporated within the  $\beta$ -Mg<sub>17</sub>Al<sub>12</sub> phase, have slightly increased the melting point of the latter phase.<sup>[35]</sup> This is in agreement with the observed higher precipitation temperatures in the cooling curves of the RE-containing alloys, as compared to the base alloy. It is interesting to note that the maximum improvement in the melting point belongs to the La-containing alloy.

The optical micrographs of the base alloy as well as those of the alloys containing Gd, Y, and La before and after exposure to 400 °C for 4, 24 and 96 hours, are shown in Figure 4. It can be deduced that the microstructures of all as-cast alloys shown in the left column of the figure are dendritic, those of the RE-containing alloys being finer than that of the RE-free base alloy. The second column of Figure 4 represents the microstructures of the alloys experiencing 4 hours annealing at 400 °C. As can be seen, the dendritic microstructures of both AZ81 and AZ81 + 1Gd alloys have completely transformed to equiaxed grain structures possessing average grain sizes of about  $80 \pm 5$  and  $60 \pm 3$   $\mu\text{m}$ , respectively. The situation is somehow different for other RE-containing alloys; the microstructure of the La-containing alloy being still dendritic and

that of the Y-containing alloy showing the onset of transformation from dendritic towards equiaxed grain structure.

Annealing for 24 hours, however, results in equiaxed recrystallized grain structures in all tested alloys, as shown in the third column of Figure 4. The base AZ81 alloy experiences the most pronounced grain coarsening with a grain size of about  $350 \pm 10 \mu\text{m}$ . In contrast to the significant change in the grain size of AZ81, the RE-containing alloys showed a less-prominent coarsening behavior, having grain sizes in the range  $30 \pm 2$  to about  $100 \pm 7 \mu\text{m}$ . By increasing the annealing time to 96 hours, a major change in the grain sizes is observed. The AZ81 alloy experiences a dramatic increase in the grain size to about  $600 \pm 10 \mu\text{m}$ , reflecting high instability of its microstructure at high working temperatures. The Gd- and Y-containing alloys also exhibit considerable grain growth and reach grain sizes of about  $400 \pm 8$ , and  $300 \pm 6 \mu\text{m}$ , respectively. Although the grain growth of the RE-containing alloys is much less than that of the AZ81 alloy, it clearly reveals the instability of these alloys at such temperatures over time. The La-containing alloy, on the other hand, shows an admirable microstructural stability in a similar

condition; exhibiting a grain size of only about  $55 \pm 4 \mu\text{m}$  after 96 hours of annealing. The general conclusion is that in all annealing conditions, the finest microstructure among the RE-containing materials belongs to AZ81 + 1La, and the coarsest structure is observed in AZ81 + 1Gd, that of the AZ81 + 1Y alloy lying in between.

The X-ray diffraction patterns of the as-cast alloys as well as those of the 96 hours annealed are depicted in Figures 5(a) through (d). As illustrated in these diffraction patterns, the  $\alpha$ -Mg and  $\beta$ -Mg<sub>17</sub>Al<sub>12</sub> intermetallic compound are the only constituents of the AZ81 alloy in the as-cast condition. On the other hand, by annealing for 96 hours, the  $\beta$ -Mg<sub>17</sub>Al<sub>12</sub> phase is dissolved in the matrix of the alloys and  $\alpha$ -Mg is the only remaining phase. The XRD patterns of the as-cast AZ81 + 1Gd (Figure 5(b)), AZ81 + 1Y (Figure 5(c)), and AZ81 + 1La (Figure 5(d)) include  $\alpha$ -Mg,  $\beta$ -Mg<sub>17</sub>Al<sub>12</sub>, and some new peaks corresponding to the Al<sub>2</sub>Gd, Al<sub>2</sub>Y, and Al<sub>11</sub>La<sub>3</sub> intermetallic compounds, respectively. The XRD patterns of the RE-containing alloys after 96 hours annealing reveal that the  $\beta$ -Mg<sub>17</sub>Al<sub>12</sub> phase has been dissolved in the matrix, but RE-rich intermetallics are still present in the microstructure. The intensities of

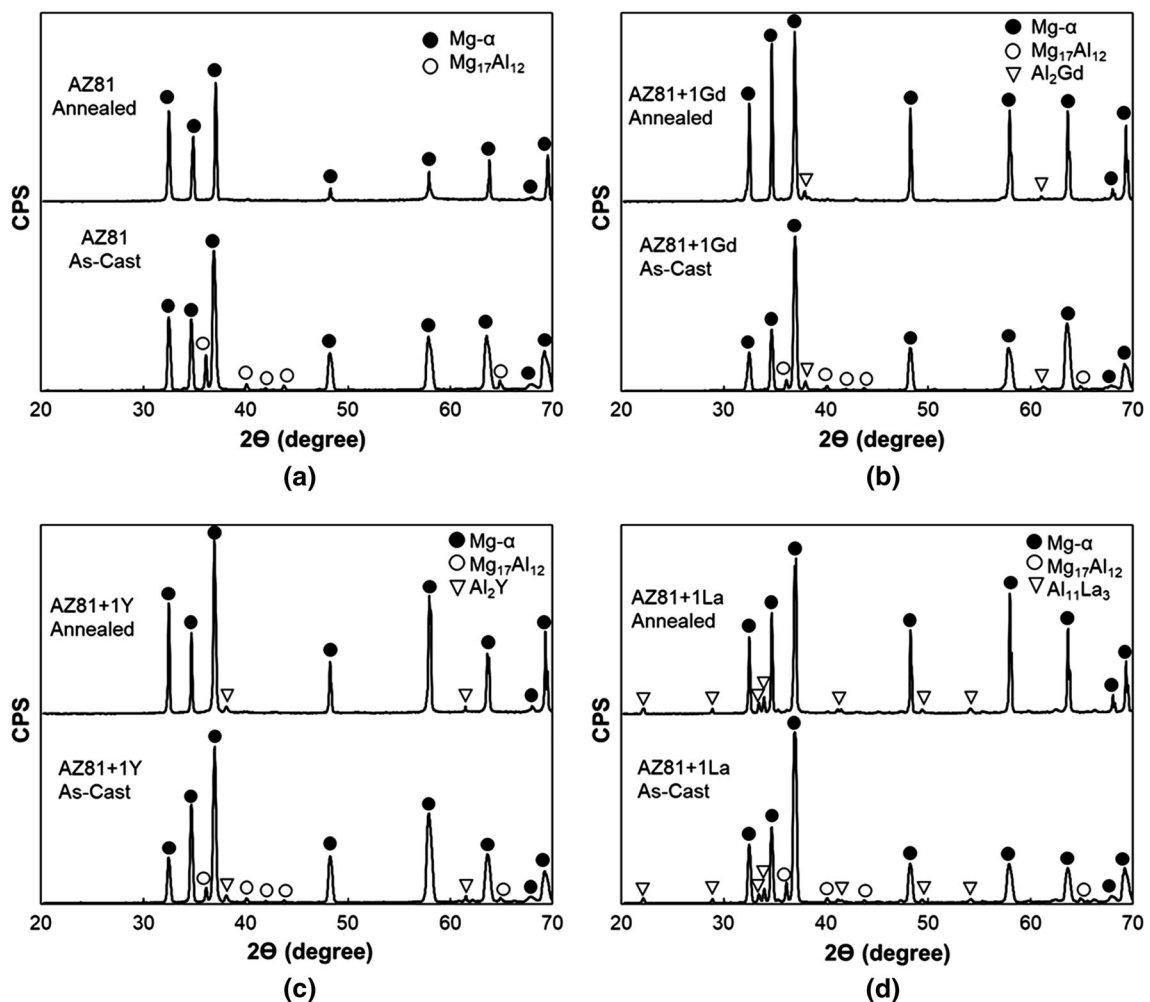


Fig. 5—XRD patterns of as-cast and 96-h annealed specimens (a) AZ81, (b) AZ81 + 1Gd, (c) AZ81 + 1Y, and (d) AZ81 + 1La.

the  $\beta\text{-Mg}_{17}\text{Al}_{12}$  peaks in the XRD patterns of the RE-containing alloys are significantly lower than those identified in the XRD pattern of the as-cast AZ81 alloy. This can be attributed to the fact that Gd, Y, and La elements consume some of the aluminum atoms to form either of  $\text{Al}_2\text{Gd}$ ,  $\text{Al}_2\text{Y}$ , and  $\text{Al}_{11}\text{La}_3$  intermetallic compounds, leaving less aluminum to be combined with the Mg matrix to form  $\beta\text{-Mg}_{17}\text{Al}_{12}$ .<sup>[18,25,28]</sup>

The dissolution of  $\beta\text{-Mg}_{17}\text{Al}_{12}$  phase in the Mg matrix can also be scrutinized by considering the exact Bragg angles of a specific Mg peak in the XRD pattern before and after annealing. A magnified view of the XRD patterns of AZ81, shown in Figure 6(a), indicates a shift in the  $\alpha\text{-Mg}$  peak from 36.8 deg in the as-cast condition to 37.1 deg after 96 hours annealing. The observed shift can be caused by the dissolution of  $\beta\text{-Mg}_{17}\text{Al}_{12}$  phase and the creation of a supersaturated solid solution of Al atoms in the Mg matrix. As such, the lattice parameter alters and results in a shift in the position of the Mg diffraction line.<sup>[36]</sup> As shown in Figures 6(b) through (d), similar peak shifts can be also observed for AZ81 + 1 Gd, AZ81 + 1Y, and AZ81 + 1La to a lesser extent, as compared to the base AZ81 alloy. This can be attributed to the lower volume fraction of  $\beta\text{-Mg}_{17}\text{Al}_{12}$

phase caused by the less available Al in the RE-containing alloys.

Examining the microstructures of the tested materials after exposure to 400 °C for 96 hours can further elucidate the dissolution of  $\beta\text{-Mg}_{17}\text{Al}_{12}$  phase. The corresponding SEM micrographs of such condition, shown in Figures 7(a) through (d), indicate the absence of  $\text{Mg}_{17}\text{Al}_{12}$  particles and the presence of non-dissolved  $\text{Al}_2\text{Gd}$ ,  $\text{Al}_2\text{Y}$  and  $\text{Al}_{11}\text{La}_3$  intermetallic particles. It worth noting that dissolution of the  $\beta\text{-Mg}_{17}\text{Al}_{12}$  intermetallic phase, under exposure to high temperatures, has frequently been reported for a variety of Mg-Al alloys.<sup>[10,11,28,37]</sup>

### C. Mechanical Properties

Figures 8(a) through (d) exhibit typical SPT curves, presented as the variation of shear stress vs normalized displacement obtained at different temperatures for the as-cast AZ81, AZ81 + 1Gd, AZ81 + 1Y, and AZ81 + 1La alloys, respectively. It can be observed that, similar to the conventional tensile stress–strain curves, after the linear elastic behavior, the curves deviate from linearity before reaching a maximum point.

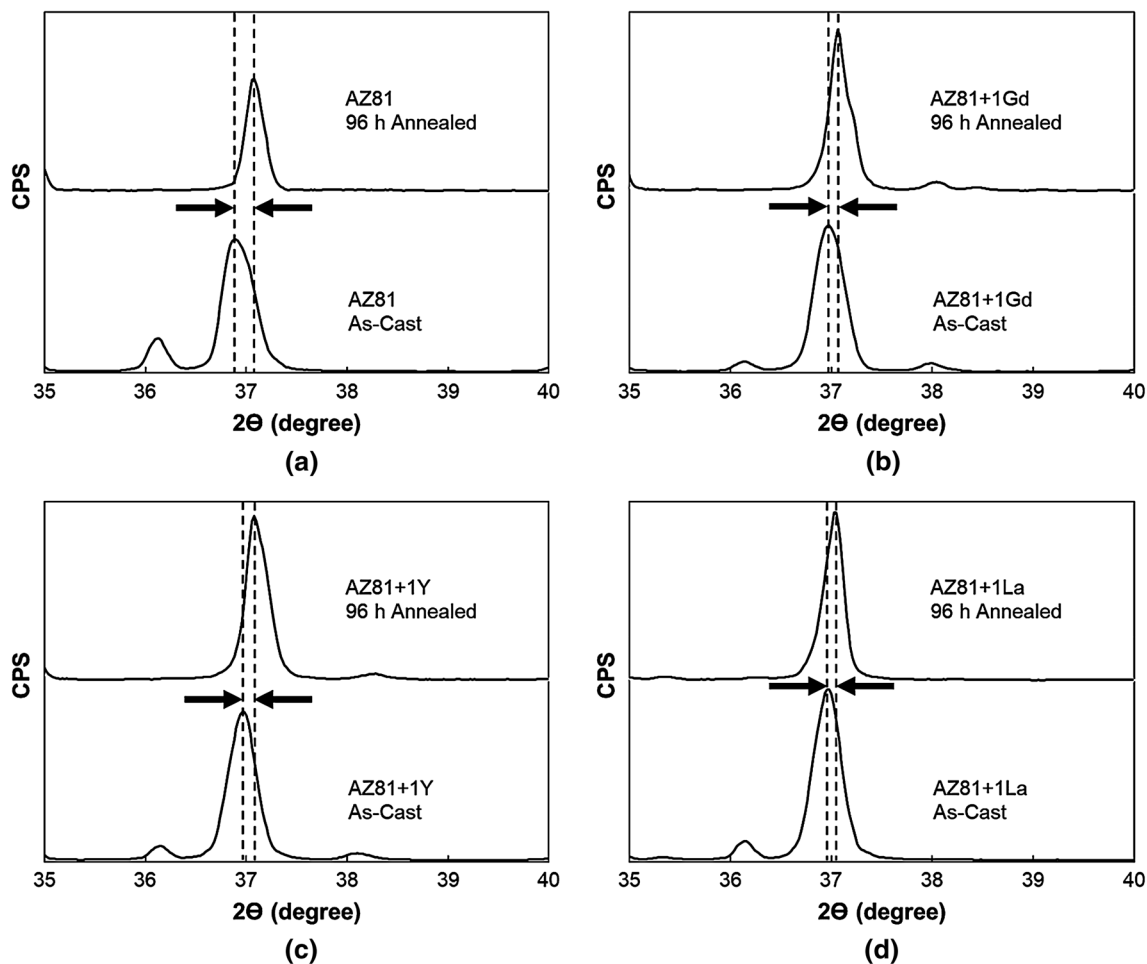


Fig. 6—Magnified views of the XRD patterns of (a) AZ81, (b) AZ81 + 1Gd, (c) AZ81 + 1Y, and (d) AZ81 + 1La, showing a shift in the  $\alpha\text{-Mg}$  peak.



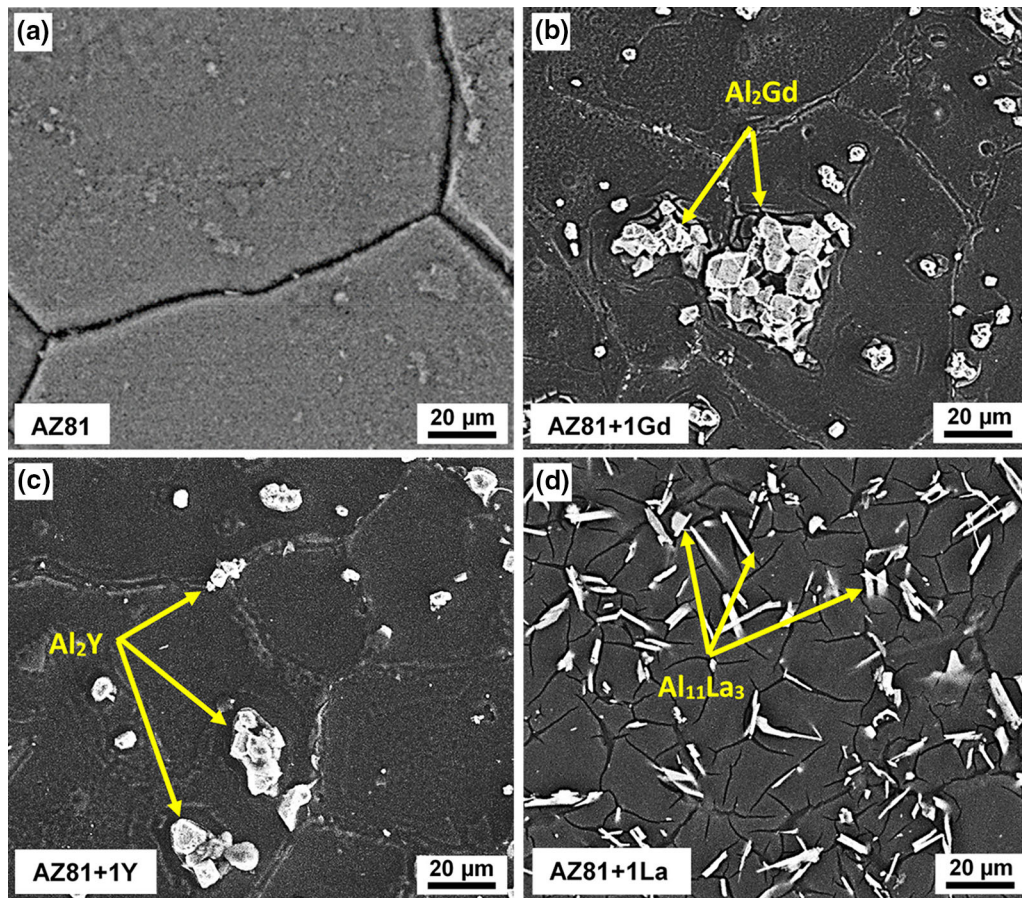


Fig. 7—SEM micrographs of 96-h annealed specimens (a) AZ81, (b) AZ81 + 1Gd, (c) AZ81 + 1Y, and (d) AZ81 + 1La.

The stress corresponding to the maximum point is referred to as the ultimate shear strength (USS). In all of the tested alloys, increasing the test temperature from 25 °C to 250 °C decreases the overall level of the flow curves; the effect being more pronounced in the base alloy.

The USS values of the alloys at different temperatures were measured to get an insight into the effects of Gd, Y, and La incorporation on the thermal stability of the AZ81 alloy. The results of this study, expressed as the variation of USS with test temperature for all materials under different annealing conditions, are depicted in Figures 9(a) through (d). The softening behavior of the as-cast specimens, exhibited in Figure 9(a), indicates that all alloys behave similarly in terms of shear strength variations with test temperature. Softening begins right above room temperature, so that there is a detectable strength drop at 150 °C in all alloys. This trend is accelerated at temperatures above 175 °C, where there is a steep drop in the strength values. Softening of the  $\beta$ -Mg<sub>17</sub>Al<sub>12</sub> phase at lower temperatures and dissolution of this phase at higher temperatures together with grain coarsening have all been responsible for the observed declines in the USS values. The superiority of the RE-containing alloys over the

base alloy is attributed to the presence of Al-RE intermetallics, as already shown in Figure 2.

The stability of the alloys after 4 hours of annealing shows some interesting results, as depicted in Figure 9(b). The curves indicate an almost flat pattern between room temperature and 150 °C, implying that there is only a trivial decline in the shear strength at 150 °C. Above 175 °C, however, the rate of strength drop increases for all alloys, the La-containing alloy having the least strength changes and the base alloy showing the most considerable strength decline. The same type of behavior is observed for the alloys after 24 and 96 hours annealing, exhibited in Figures 9(c) and (d), respectively. The only difference is that the strength decreases more rapidly with increasing temperature as the annealing temperature increases. The superiority of the 4-hour annealed alloys to the as-cast conditions can be ascribed to the simultaneous synergistic effects of significant solid solution hardening of Al in the Mg matrix, elimination of the deteriorating role of Mg<sub>17</sub>Al<sub>12</sub> at high temperatures, and retention of fine grain structure, all of which contribute to the overall strength. Obviously, the presence of the thermally stable particles of Al<sub>2</sub>Gd, Al<sub>2</sub>Y, and Al<sub>11</sub>La<sub>3</sub> in the RE-containing alloys can further help in retaining the strength at high

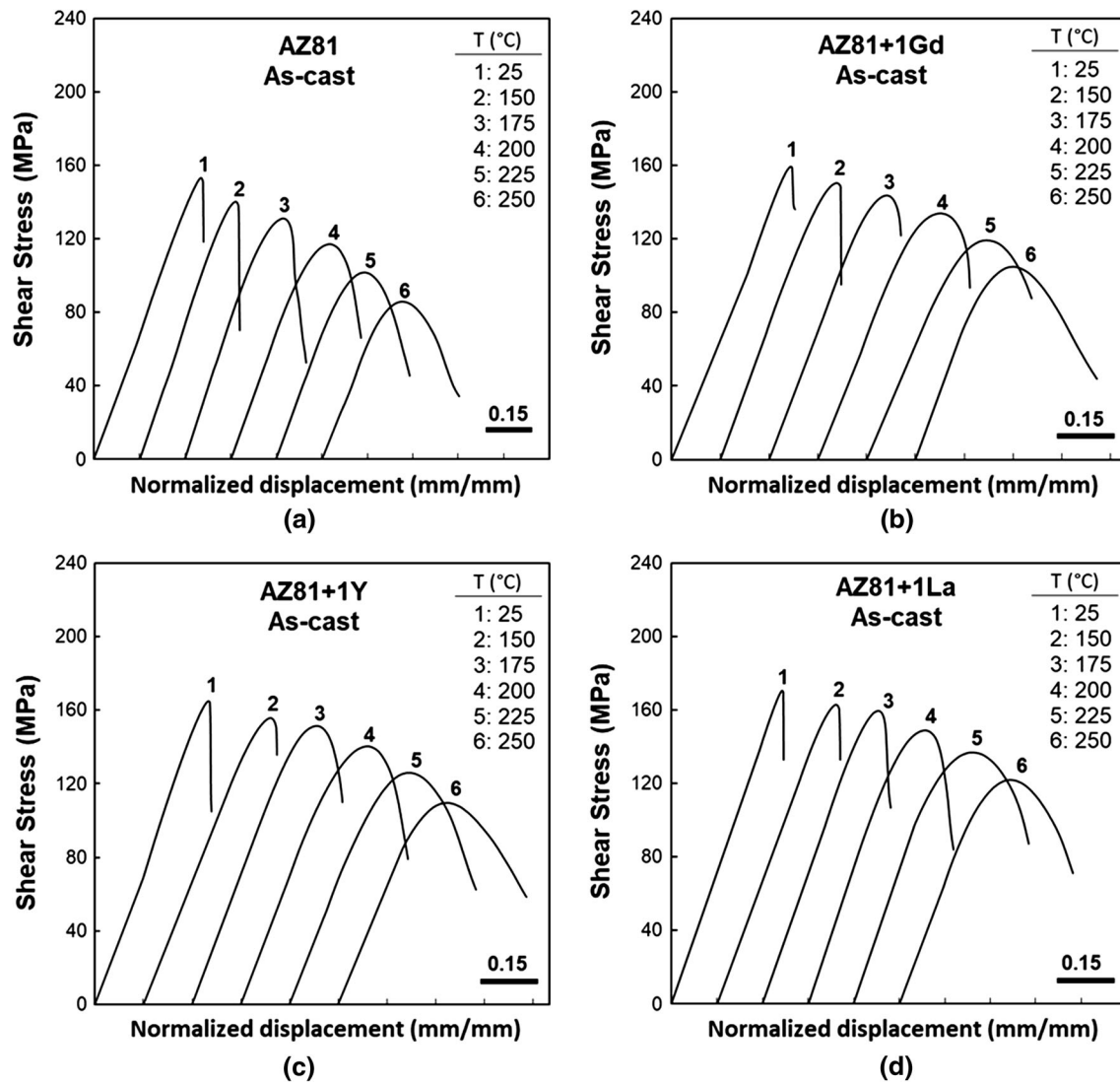


Fig. 8—Typical SPT curves for the as-cast: (a) AZ81, (b) AZ81 + 1Gd, (c) AZ81 + 1Y, and (d) AZ81 + 1La.

temperatures. In addition to having relatively high melting points, these particles consume the Al content of the alloys and suppress the formation of  $Mg_{17}Al_{12}$  particles, both of which contribute to the retention of strength at elevated temperatures.<sup>[25,32]</sup>

At longer annealing times of 24 and 96 hours, the overall levels of the curves are lowered due to the coarsening of the grain structure, already viewed in Figure 4. It is worth noting that the gap between the curves for the La-containing alloy and other alloys, especially the base alloy, has become wider. This reflects the high-microstructural stability of the AZ81 + 1La alloy, caused by the  $Al_{11}La_3$  particles and the refined grain structure shown in Figure 7(d). It seems that  $Al_2Gd$  and  $Al_2Y$  particles have not been as effective as  $Al_{11}La_3$  in the pinning of the grain boundaries and prevention of grain growth.<sup>[10,11,25,31]</sup> This stems from the higher volume fraction and a more uniform dispersion of the  $Al_{11}La_3$  particles respect to  $Al_2Gd$  and  $Al_2Y$

particles. Moreover, the formation of  $Al_{11}La_3$  phase is accompanied by substantial consumption of the Al content of the base alloy, and thus, further suppression of  $Mg_{17}Al_{12}$  formation.<sup>[28,31]</sup>

#### IV. SUMMARY AND CONCLUSION

1. The microstructure of the base AZ81 alloy, which consists of  $Mg_{17}Al_{12}$  intermetallic phase in the Mg matrix, undergoes extensive grain coarsening when exposed to high temperatures. Separate additions of 1 wt pct Gd, Y, and La rare-earth (RE) elements refined the dendritic structure of the as-cast alloy, decreased the volume fraction of the  $\beta$ - $Mg_{17}Al_{12}$  phase, and resulted in the formation of  $Al_2Gd$ ,  $Al_2Y$ , and  $Al_{11}La_3$  intermetallic particles, respectively.

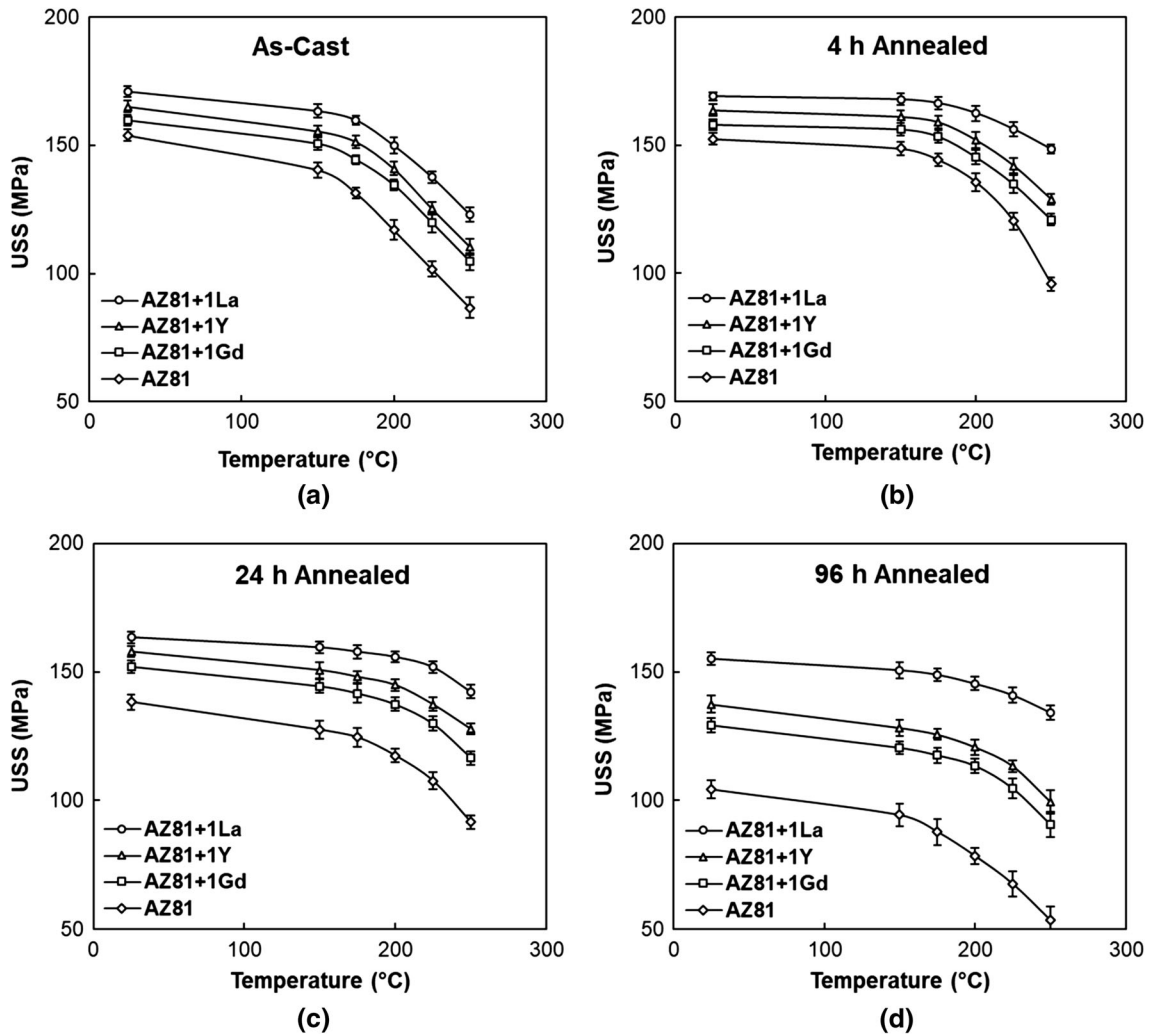


Fig. 9—The USS of AZ81, AZ81 + 1Gd, AZ81 + 1Y, and AZ81 + 1La alloys at 25 °C to 250 °C for the (a) as-cast, (b) 4-h annealed, (c) 24-h annealed, and (d) 96-h annealed specimens.

- All of the RE-containing alloys exhibited enhanced microstructural stabilities in comparison with the AZ81 base alloy. The observed improvement can be ascribed to the formation of the thermally stable cuboid  $Al_2Gd$  and  $Al_2Y$  particles, as well as the acicular  $Al_{11}La_3$  particles, which act as barriers inhibiting the grain coarsening throughout the annealing treatment at 400 °C.
- The microstructural stability of the studied alloys affected their shear strength at elevated temperatures and after long-term annealing. All three added RE elements significantly enhanced the strength of the base alloy in both as-cast and annealed conditions. This stemmed from their microstructural refinement capacity, high thermal stability, hardening effects, and diminishing of the weak  $Mg_{17}Al_{12}$  volume fraction. The most effective element was La, which produced the thermally stable  $Al_{11}La_3$  particles, resisting softening and dissolution upon exposure to high temperatures and during annealing treatments.

## REFERENCES

- I.J. Polmear: *Light Alloys*, 2nd ed., Chapman and Hall Inc, New York, 1989, pp. 170–88.
- Z. Yang, J.P. Li, J.X. Zhang, G.W. Lorimer, and J. Robson: *Acta Metall. Sinica*, 2008, vol. 21, pp. 313–28.
- K.U. Kainer: *Magnesium Alloys and Technology*, Wiley, Weinheim, 2003, pp. 1–23.
- A. Luo and M.O. Pekguleryuz: *J. Mater. Sci.*, 1994, vol. 29, pp. 5259–71.
- E. Aghion, B. Bronfin, F. Von Buch, S. Shumann, and H. Friedrich: *JOM*, 2003, vol. 55, pp. 30–33.
- R. Alizadeh and R. Mahmudi: *Mater. Sci. Eng.*, 2010, vol. 527A, pp. 5312–17.
- G. Nayyeri and R. Mahmudi: *Mater. Des.*, 2011, vol. 32, pp. 1571–76.
- H.K. Lim, S.W. Sohn, D.H. Kim, J.Y. Lee, W.T. Kim, and D.H. Kim: *J. Alloys Compd.*, 2008, vol. 454, pp. 515–22.
- Y. Chen, L. Jin, D. Fang, Y. Song, and R. Ye: *J. Rare Earths*, 2015, vol. 33, pp. 86–92.
- B. Kondori and R. Mahmudi: *Mater. Sci. Eng.*, 2010, vol. 527A, pp. 2014–21.
- F. Kabirian and R. Mahmudi: *Adv. Eng. Mater.*, 2009, vol. 11, pp. 189–93.

12. R. Alizadeh, R. Mahmudi, A.H.W. Ngan, P.H.R. Pereira, Y. Huang, and T.G. Langdon: *Metall. Mater. Trans. A*, 2016, vol. 47A, pp. 6056–65.
13. N. Bayat Tork, S.H. Razavi, H. Saghaian, and R. Mahmudi: *Adv. Eng. Mater.*, 2016, vol. 18, pp. 156–61.
14. X. Wang, W. Du, K. Liu, Z. Wang, and S. Li: *J. Alloys Compd.*, 2012, vol. 522, pp. 78–84.
15. K.J. Li: *Adv. Mater. Res.*, 2013, vol. 821, pp. 860–63.
16. R. Alizadeh, R. Mahmudi, A.H.W. Ngan, and T.G. Langdon: *J. Mater. Sci.*, 2015, vol. 50, pp. 4940–51.
17. Y. Ali, D. Qiu, B. Jiang, F. Pan, and M.X. Zhang: *J. Alloys Compd.*, 2015, vol. 619, pp. 639–51.
18. N. Jiang, L. Chen, L. Meng, C. Fang, H. Hao, and X. Zhang: *J. Rare Earths*, 2016, vol. 34, pp. 632–37.
19. M.F. Wang, D.H. Xiao, P.F. Zhou, W.S. Liu, Y.Z. Ma, and B.R. Sun: *J. Alloys Compd.*, 2018, vol. 742, pp. 232–39.
20. J. Zhang, X. Niu, X. Qiu, K. Liu, Ch. Nan, D. Tang, and J. Meng: *J. Alloys Compd.*, 2009, vol. 471, pp. 322–30.
21. E. Aghion, Y. Gueta, N. Moscovitcha, and B. Bronfin: *J. Mater. Sci.*, 2008, vol. 43, pp. 4870–75.
22. Z. Zhao, Q. Chen, Y. Wang, and D. Shu: *Mater. Sci. Eng.*, 2009, vol. 515A, pp. 152–61.
23. A. Bobby, A. Srinivasan, U.T.S. Pillai, and B.C. Pai: *Mater. Des.*, 2015, vol. 88, pp. 871–79.
24. M. Wang, H. Zhou, and L. Wang: *J. Rare Earths*, 2007, vol. 25, pp. 233–37.
25. N. Kashefi and R. Mahmudi: *Mater. Des.*, 2012, vol. 39, pp. 200–10.
26. G. Wu, Y. Fan, H. Gao, C. Zhai, and Y.P. Zhu: *Mater. Sci. Eng.*, 2005, vol. 408A, pp. 255–63.
27. D. Wenwen, S. Yangshan, M. Xuegang, X. Feng, Z. Min, and W. Dengyun: *Mater. Sci. Eng.*, 2003, vol. 356A, pp. 1–7.
28. R. Mahmudi, F. Kabirian, and Z. Nematollahi: *Mater. Des.*, 2011, vol. 32, pp. 2583–89.
29. H. Liao, S. Long, C. Guo, and Z. Zhu: *Trans. Nonferrous Met. Soc. China*, 2008, vol. 18, pp. 44–49.
30. F. Khomamizadeh, B. Nami, and S. Khoshkhouei: *Metall. Mater. Trans. A*, 2005, vol. 36A, pp. 3489–94.
31. F. Kabirian and R. Mahmudi: *Metall. Mater. Trans. A*, 2009, vol. 40A, pp. 2190–2201.
32. N. Ishimatsu, Y. Terada, T. Sato, and K. Ohori: *Metall. Mater. Trans. A*, 2006, vol. 37A, pp. 243–48.
33. S. Golmakaniyoon and R. Mahmudi: *Mater. Sci. Eng.*, 2011, vol. 528A, pp. 1668–77.
34. A.L. Allred: *J. Inorg. Nucl. Chem.*, 1961, vol. 17, pp. 215–21.
35. N. Balasubramani, A. Srinivasan, U.T.S. Pillai, and B.C. Pai: *Mater. Sci. Eng.*, 2007, vol. 457A, pp. 275–81.
36. B.D. Cullity: *Element of X-Ray Diffraction*, Addison-Wesley, Reading, 1956, p. 347.
37. B. Kondori and R. Mahmudi: *Metall. Mater. Trans. A*, 2009, vol. 40A, pp. 2007–15.

**Publisher's Note** Springer Nature remains neutral with regard to jurisdictional claims in published maps and institutional affiliations.